

# Modelling ultra-high frequency x-ray emission in particle in cell codes

Miguel Pardal  
miguel.j.pardal@ist.utl.pt

Instituto Superior Técnico, Lisboa, Portugal

October, 2018

## Abstract

Radiation processes in plasma are extremely relevant for a number of fields ranging from astrophysics to small scale microscopy. These processes are usually associated with the motion of many individual electrons, where collective plasma effects can be important. Thus, their understanding requires numerical modelling. In particular, Particle In Cell codes are able to accurately describe the motion of the individual particles but fail to capture the radiation due the difference between the temporal scales of the particle's motion and the emitted radiation. This work describes a new radiation diagnostic that captures the unexplored spatiotemporal properties of radiation, which is potentially useful in the discovery of specific astrophysical scenarios or the enhancement of radiation sources. The algorithm is ideal to describe the radiation from many particles and has been fully integrated into the particle-in-cell code OSIRIS, being now ready to be applied to any radiation emission scenario. This algorithm allows the detector to have an arbitrarily high temporal resolution without significantly affecting the computational load. The tool is shown to recover the theoretical spectra for well-known scenarios of radiation emission with decent parallel performance in some of the world's largest supercomputers and was used to compute the spatiotemporal profile of betatron radiation in plasma accelerators. The implications of the use of macroparticles in the simulation are also studied and a method to recover the laboratory results is proposed.

**Keywords:** Radiation, Plasma, Parallel Computing, Simulation, Detector

## 1. Introduction

Plasma based radiation sources are ubiquitous both in astrophysical scenarios and cutting-edge radiation generating devices here on earth. Be it from a plasma set in motion by a highly rotating black hole [1] or from a compact High Harmonic Generation (HHG) device [2], this sort of radiation has unique properties in both the spatiotemporal and spectral domains which can be used to accurately identify distant events or further enhance radiation generation techniques.

The processes behind radiation emission in plasmas result from strongly non-linear many body interactions which involve relativistic effects, so they are best modeled through Particle-In-Cell[3] (PIC) simulations. However, capturing this radiation directly in PIC simulations is very challenging due to the large disparity between the temporal and spatial scales associated with such phenomena, as the frequency of the emitted radiation  $\omega_{rad}$ , scales with the typical frequency of the particle's motion  $\omega_p$  multiplied by the particle's squared Lorentz factor,  $\gamma_p^2$ , which can be of the order of  $10^4$  or higher for extremely relativistic particles.

$$\omega_{rad} \propto \omega_p / \gamma_p^2 \quad (1)$$

Current algorithms only describe radiation processes in the Fourier space (e.g. JRAD [4], PIConGPU [5]),

missing the spatiotemporal features of the emitted radiation, which can be equally crucial to many fields. The Liénard-Wiechert potentials [6] (see Equation (2)), which model radiation emission by moving charges, are the most commonly adopted strategy to capture the emitted radiation without having to increase the PIC resolution to a point where simulations become unfeasible. They can be used to calculate the value of the emitted electromagnetic fields at certain regions of space. These regions, henceforth referred to as *detector*, may be arbitrarily discretized in both space and time independently of the PIC resolution.

$$\begin{aligned} \mathbf{E}(\mathbf{x}, t) &= e \left[ \frac{\mathbf{n} - \boldsymbol{\beta}}{\gamma^2 (1 - \boldsymbol{\beta} \cdot \mathbf{n})^3 R^2} \right]_{\text{ret}} \\ &+ \frac{e}{c} \left[ \frac{\mathbf{n} \times [(\mathbf{n} - \boldsymbol{\beta}) \times \dot{\boldsymbol{\beta}}]}{(1 - \boldsymbol{\beta} \cdot \mathbf{n})^3 R} \right]_{\text{ret}} \\ \mathbf{B}(\mathbf{x}, t) &= [\mathbf{n} \times \mathbf{E}]_{\text{ret}} \end{aligned} \quad (2)$$

Equation (2) contains the expressions for the emitted electric,  $\mathbf{E}$ , and magnetic,  $\mathbf{B}$ , fields at a given position,  $x$  and time  $t$ , calculated from quantities obtained at the retarded time of emission, hence the subscript *ret*. The quantities  $\mathbf{n}$ ,  $\boldsymbol{\beta}$  and  $\dot{\boldsymbol{\beta}}$ , are respectively the direction vector from the radiation emitting particle to

the detector, the normalized velocity,  $v/c$ , and the normalized acceleration, as shown in Figure 1.  $R$  is the total distance from the particle to the detector at the time of emission,  $t_{\text{ret}}$ . For a sufficiently distant detector  $R^2 \gg R$  and the first term of Equation (2) can be dropped, leaving only the so-called acceleration fields.  $e$  and  $c$  are respectively the electron's charge and the speed of light.

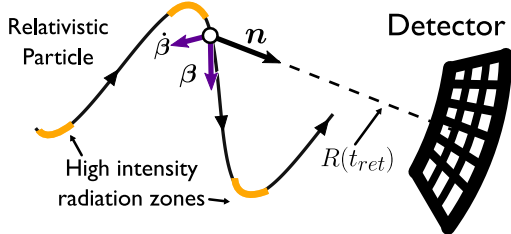


**Figure 1:** Illustration of the geometry of the radiation emission process and relevant quantities.

This work follows the implementation, benchmarking and testing of a diagnostic that is able to calculate the emitted radiation in the spatiotemporal domain, called RaDiO, the Radiation Diagnostic for OSIRIS. This diagnostic is composed of two distinct but equally useful counterparts: one implemented as a post-processing tool that uses previously generated trajectories to find the radiation that was emitted along them, and the other implemented as a run-time diagnostic for the PIC code OSIRIS [7], that uses the simulation data at each time step to compute the radiation.

The run-time diagnostic is able to compute the radiation of a large number of particles in a single run ( $10^5$ ), which is an advantage over the post-processing tool, as the latter requires that the particle's trajectories be stored in memory, which becomes unfeasible for such large number of particles. On the other hand, if one desires to quickly tweak the detector's configuration, the post-processing tool is more desirable as it does not require running a full PIC simulation to obtain radiation results.

## 2. Implementation Details

### 2.1. Numerical model

Equation (2) suggests that, for each time slot of the detector, the fields should be calculated by finding the corresponding time of the particle's trajectory ( $t_{\text{ret}}$ ) and then use the position and momenta at that time. However, this is not feasible in a run-time scenario as it would require knowledge of the full trajectories, which is only available after the simulation is run.

The correct strategy is therefore to do the inverse operation: for each time-step of the simulation, compute the time at which the radiation arrives at the detector ( $t = t_{\text{det}}$ ) and then use the available simulation quantities to compute and deposit the electromagnetic field, as shown in the following equation:

$$\begin{aligned} \mathbf{E}(\mathbf{x}, t = t_{\text{det}}) &= \frac{e}{c} \left[ \frac{\mathbf{n} \times [(\mathbf{n} - \boldsymbol{\beta}) \times \dot{\boldsymbol{\beta}}]}{(1 - \boldsymbol{\beta} \cdot \mathbf{n})^3 R} \right]_{t=t_{\text{ret}}}, \\ \mathbf{B}(\mathbf{x}, t = t_{\text{det}}) &= [\mathbf{n} \times \mathbf{E}]_{t=t_{\text{ret}}} \end{aligned} \quad (3)$$

This strategy, which can be implemented in both the run-time and post-processing version, is summarized in Algorithm 1. It comprises two different loops: one through all the radiative particles and another through the detector's cells that are both potentially parallelizable.

---

### Algorithm 1 Radiation calculation and depositing

---

```

1: procedure RADIATIONCALCULATOR
2:   for all cell in detector do
3:     for all particle in simulation do
4:        $\mathbf{n} \leftarrow \text{direction}(\text{particle}, \text{cell})$ 
5:        $\boldsymbol{\beta} \leftarrow \text{velocity}(\text{particle})$ 
6:        $\dot{\boldsymbol{\beta}} \leftarrow \text{acceleration}(\text{particle})$ 
7:        $R \leftarrow \text{distance}(\text{particle}, \text{cell})$ 
8:        $t_{\text{arrive}} \leftarrow R/c + t$ 
9:       if  $t_{\text{det}}^{\text{min}} < t_{\text{det}} < t_{\text{det}}^{\text{max}}$  then
10:         $\mathbf{E}(\text{cell}, t_{\text{arrive}}) \leftarrow \mathbf{E}(\mathbf{n}, \boldsymbol{\beta}, \dot{\boldsymbol{\beta}})$ 

```

---

The calculation of the time of arrival,  $t_{\text{det}}$ , may be simplified for performance purposes if the detector is far enough from the particle, at the so-called far-field regime:

$$t_{\text{det}} = t_{\text{ret}} + R_{\text{cell}} - \mathbf{r}_{\text{part}} \cdot \mathbf{n}_{\text{cell}} \quad (4)$$

In OSIRIS, the information about the particles is stored in objects of the class *species*. These objects contain information about the particles' instantaneous state but the radiation algorithm requires information about the *previous* state of the particles.

As evidenced by Equation (3), computing the emitted radiation requires information about the acceleration of the particle, which can only be obtained using the velocity of the particle at the previous time step.

In order to cope with this requirement, Fortran 90 enables the creation of an extension of the *species* class, whose objects contain all attributes and procedures of the original class as well as additional members that may be defined. In this way, a new class called *species\_radiat* was created in OSIRIS. Objects of this species contain data on the previous position and momentum as well as the methods to calculate and deposit electromagnetic radiation in the detector object.

### 2.2. Detector

The virtual detector is a key feature of the radiation diagnostic. It is the region of space where radiation is tracked during a given time period. This time period is usually different from the simulation time, as

the detector often needs to have a higher temporal resolution than the PIC simulation. This way, it can be defined as a 4-D grid with any given shape. Two types of detectors were implemented (Figure 2): a spherical one, where the grid is defined using spherical coordinates  $(\mathbf{e}_\theta, \mathbf{e}_\phi, \mathbf{e}_r)$  and a cartesian one, where the grid is defined using cartesian coordinates  $(\mathbf{e}_x, \mathbf{e}_y, \mathbf{e}_z)$ .

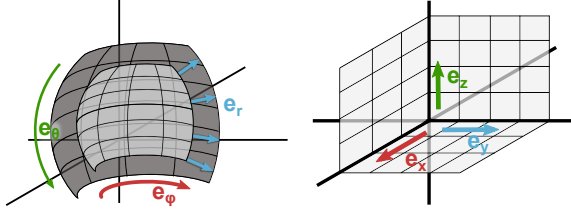


**Figure 2:** Spherical (left) and cartesian (right) detectors. The darker spherical grid has a higher radius than the lighter one. All spherical grids are centered in the origin of the coordinate system.

In each step of the simulation (or the trajectory, in the post-processing code), the radiation algorithm loops through the spatial cells of the detector, finding the correct time cell for depositing the calculated radiation. However, it is highly unlikely that the deposition time matches the discretized time grid of the Detector. Therefore, in order to figure out exactly how much radiation should be deposited in each time slot, an interpolation is required.

### 2.3. Deposition of the radiated fields

In OSIRIS, the calculation and deposition of the emitted radiation take place in a sub-step of the PIC loop created specifically for that purpose. As shown in Figure 3, this sub-step comes right after pushing the particles, in such a way that the newly calculated positions and velocities can be used to compute the required quantities for radiation calculation. In the post-processing version, each step of the trajectory corresponds to a full PIC loop, and the code computes the radiation at each trajectory step as it loops through the track.

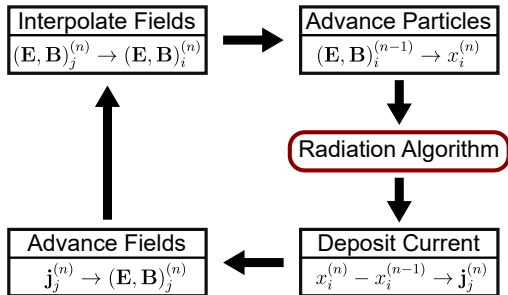


**Figure 3:** Modified PIC loop with the addition of the radiation calculation procedure.

In the likely event that the time of deposition does not match any of the discretized time steps of the detector, an interpolation must be performed in order to

deposit the fields across different detector cells. The simplest method would be the so called *closest point approximation*, which consists in depositing the radiation fields at the closest time step. In spite of its simplicity, this strategy, which corresponds to an instantaneous detector, may lead to some problems, such as conflicting values or double counting when radiation is deposited two or more times in the same time slot.

These issues can be avoided with an *integrator* detector, which weighs the contribution of each deposition by the time until the next deposition. Therefore, the value of the radiation in a time slot is the integral of the radiation in the interval delimited by two consecutive time-steps, similar to what a real detector would do. Figure 4 shows an example case that clarifies this deposition scheme.

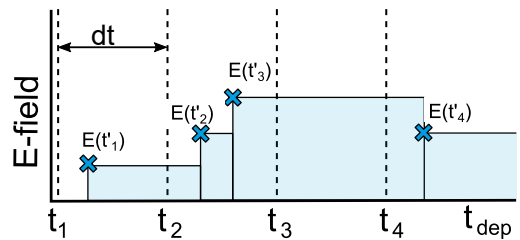


**Figure 4:** Integrator detector: radiation is scaled by the time until the next deposition.  $t_i$  refers to the detector's time grid and  $t'_i$  to the different deposition times.

Each of these depositions corresponds to radiation emitted at different simulation time steps. In this context, this interpolation can be performed while the simulation is running as it only requires information about the radiated field in the previous time step. In fact, for the example present in Figure 4 the deposition algorithm would go as described below for iteration 2 (second cross from the left):

- The radiation arrives at the detector at  $t = t'_2$ .  
 $E(t'_1)(t_2 - t'_1)/dt$  is deposited in the first time slot,  $t_1$ .  
 $E(t'_1)(t'_2 - t_2)/dt$  is deposited in the second time slot,  $t_2$ .

Using this approach, radiation can be computed and deposited using only the information from the current and the previous time steps. The fields are always calculated at the previous time step using the previous position and momentum and the integration is accomplished using the previous deposition time.

### 2.4. Parallelization

The radiation algorithm consists in two loops, one that circles through the  $N_p$  particles and another one that, for each particle, circles through the  $N_c$  detector cells, performing  $\sim N_p N_c$  operations. While the particle loop can only be parallelized using distributed memory parallelization due to concurrence problems that

arise when two or more particles deposit radiation in the same detector object, the detector loop can be parallelized using shared memory parallelization.

The parallelization scheme in OSIRIS is illustrated in Figure 5. It consists in dividing the simulation domain in segments, assigning each segment to a single processor, in such a way that each processor only deals with a specific region of space. Informations about the particles that cross regions and the fields or currents at the boundaries are shared between processors using the MPI message passing interface. A mixture of shared and distributed memory parallelization using OpenMP together with MPI is also supported, but in general, only MPI is used.

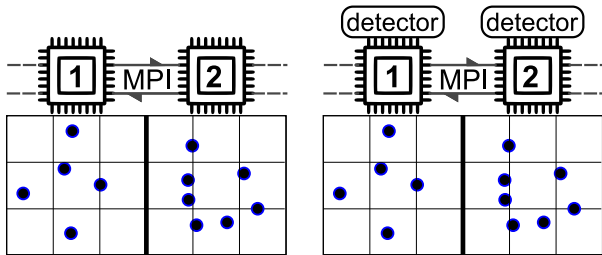


**Figure 5:** Comparison between the standard OSIRIS parallelization (left) and the parallelization of the radiation diagnostic (right). Each of the represented CPU's may have multiple cores that can be used to further parallelize operation in each sub-region using OpenMP. This cluster architecture is fairly common in current supercomputers.

This diagnostic uses a parallelization scheme that exploits this domain decomposition by assigning a copy of the detector to each sub-domain (Figure 5, right). In this way, each Distributed Memory Processor (DMP) deals with the radiation emitted by the particles inside its assigned region. In the post-processing code, the particles in each sub-group are not bound to a specific region, as they are grouped by order of appearance in the trajectory file.

Before the code writes the detector in memory, each copy is summed into a single detector using MPI. This method almost fully avoids communications between processors during the rest of the simulations and therefore should not affect the overall parallel efficiency.

Distributed-shared memory hybrid parallelization was also implemented, but kept as an optional feature. The main difference from the previous code is that instead of assigning a single DMP to a sub-group of particles, several Shared Memory Processors (SMP) are used to calculate the radiation of the particles present in a sub-group using a single detector which is split among the SMPs. In this way, if the total number of processors is kept constant, the number of region sub-domains decreases, which leads to a decrease in the amount of memory and communications required when compared to the previous scheme. In theory, this does not lead to a loss of parallel efficiency as in both cases each processor deals with the same amount of radia-

tion calculation operations, however this is only true for radiation calculations as not all other steps in the PIC loop can be parallelized with shared memory, often resulting in an increase of operations per processor.

### 3. Benchmarking and Performance

The spatiotemporal behaviour of the radiation emitted by charged particles either in a plasma medium or a synchrotron environment remains fairly unexplored and to the best of our knowledge, no theoretical predictions have been made on the spatiotemporal signature of any kind of motion. However, the spectral properties of radiation are well documented for some common types of motion. These spectra can be obtained by performing a Fast Fourier Transform (FFT) on the spatiotemporal detector, making it possible to benchmark the results against the theoretical predictions for the radiated spectrum.

Typical synchrotron light sources generate radiation by making relativistic particles undergo a sinusoidal or helical motion inside periodic magnetic structures known as *wigglers* or *undulators*. Such conditions can also be obtained in a plasma medium using relativistic plasma waves [8] instead of magnetic structures.

In this way, several radiation favorable scenarios have been idealized and thoroughly studied to the point where accurate theoretical predictions can be made. The conditions required for these predictions to hold are usually not met in collective systems of particles, as the interactions between them normally affect their trajectories, introducing deviations from the ideal conditions. As a result, these tests were performed with artificially-generated single-particle trajectories via the post-processing radiation diagnostic. Furthermore, the run-time radiation diagnostic was benchmarked against the post-processing code by comparing the radiation obtained directly from an OSIRIS run with the radiation obtained from the trajectories originated by the same run.

#### 3.1. Sinusoidal trajectory

Most wiggler and undulator mechanisms inside synchrotron devices impose a sinusoidal trajectory to the relativistic electron beam in order to obtain high energy, coherent radiation. The spectrum of the emitted radiation is given by the following Equation [9], which is only valid for extremely relativistic particles ( $\gamma \gg 1$ ):

$$\frac{d^2 I}{d\omega d\Omega} = \frac{e^2 \omega^2 \gamma^2}{3\pi^2 c \omega_\beta K} \left( \frac{1}{\gamma^2} + \theta^2 \right)^2 \times \left[ \frac{\theta^2}{\gamma^{-2} + \theta^2} K_{2/3}^2(\Upsilon) + K_{1/3}^2(\Upsilon) \right], \quad (5)$$

where  $\omega_\beta$  is the frequency of the sinusoid,  $\theta$  is the observation angle in the direction perpendicular to the trajectories plane. The  $K_n$  functions are the

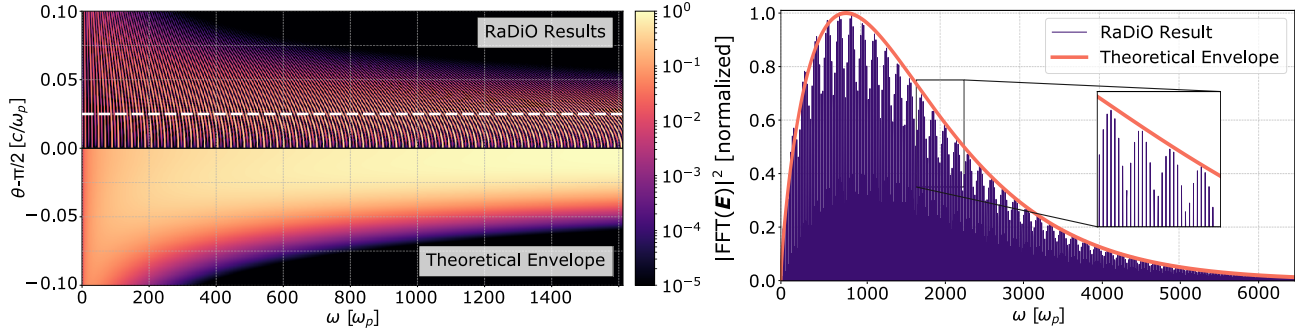


**Figure 6:** a) Comparison between the theoretical and simulated spectra. b) Comparison between a lineout at  $\Delta\theta = 0.02$  from both spectra. This detector had 512 spatial cells and 131072 temporal cells, resulting in a temporal resolution of  $2.98 \times 10^{-5} c/\omega_p$

modified Bessel functions and  $\Upsilon$  is given by  $\Upsilon = \frac{\omega\gamma}{3\omega_\beta K} (\gamma^{-2} + \theta^2)^{-3/2}$ . Finally,  $K$  is a trajectory parameter that can be taken as a scaled pitch angle, the maximum angle of the particle trajectory, scaled by the Lorentz factor  $\gamma$ . Therefore,  $K = \gamma r_b \omega_\beta / c$ , where  $r_b$  is the trajectory amplitude.

Equation (5) can be integrated over all angles, returning the frequency spectrum:

$$\frac{dI}{d\omega} = \sqrt{3} \frac{e^2 \gamma \omega}{c \omega_c} \int_{\omega/\omega_c}^{\infty} K_{5/3}(x) dx, \quad \omega_c = \frac{3}{2} \gamma^2 \omega_\beta \quad (6)$$

The benchmarks were performed using the two dimensional sinusoidal trajectory of an ultra-relativistic electron ( $\gamma = 50$ ) with an amplitude of  $2c/\omega_p$  and  $k_0 = 0.1\omega_p/c$  ( $K = 10$ ) in the  $x_1x_2$  plane. This trajectory was then analyzed with the post-processing code using a slice of a spherical detector, placed in the  $x_3x_1$  plane,  $10^5 c/\omega_p$  away from the axis origin with an angular aperture of 0.1 rad around the  $x_1$  axis.

The comparison with the theoretical predictions presented in Equation (5) was achieved by taking the FFT of each field component with respect to time for each angular slice of the detector and then summing the components to obtain  $|\text{FFT}(\mathbf{E})|^2$ . The results are displayed in Figure 6. As the spectrum is symmetric with respect to  $\theta$ , the comparison can be easily made by representing the two complementary halves of both the theoretical and simulated spectrum (upper left).

Although both spectra feature exactly the same shape, there are notable differences as the theoretical prediction seems to be much smoother than the simulation results. This can be evidenced by the lineout displayed in the right panel, where the theoretical line is shown to be a smooth curve that envelopes the simulation results. This happens because the result on equation (5) comes from an asymptotic expression valid only for  $\gamma \rightarrow +\infty$ ,  $K \gg 1$  and a very large number of periods in the trajectory, ultimately corresponding to a superposition of harmonics.

Moreover, the integration of the spectrum over all angles yields the frequency distribution of the emitted radiation which can be benchmarked against Equation (6). In order to make this comparison, a peak detection

algorithm was applied to the results and the relative error between the envelope and the detected peaks was measured (Figure 7). The result is very good as the intensity of most peaks matches the expected result with small relative error which rises as frequency increases.

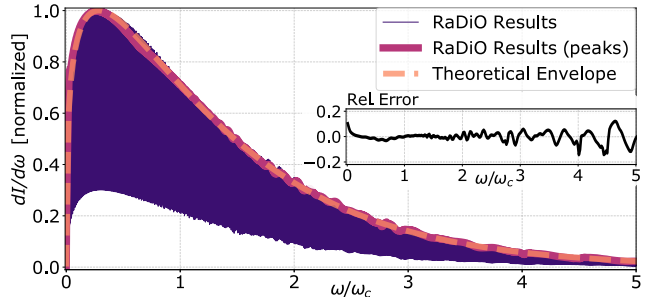


**Figure 7:** Angle integrated spectra, both spectra are normalized to 1. The relative error is shown on the inset.

Since there is no trivial expression for the frequency integrated spectrum,  $dI/d\Omega$ , this result was benchmarked against the spectrum provided by the post-processing spectral code JRad. The results are once again very good as they show great agreement between the outputs of both codes (Figure 8).

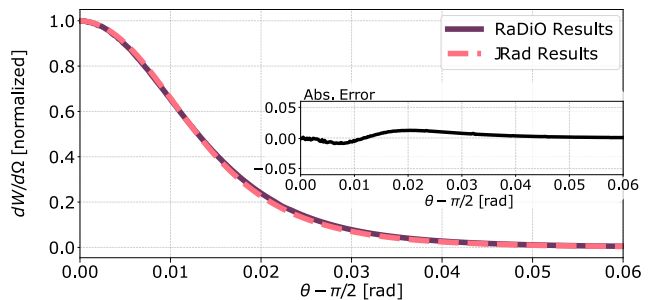


**Figure 8:** Frequency integrated spectra, both spectra are normalized to 1. The absolute error is shown on the inset.

### 3.2. Helical trajectory

The helical trajectory, which can be seen as a composition of two sinusoidal trajectories in perpendicular planes, was first proposed as an alternative to the conventional sinusoid, potentially yielding an improvement of several orders of magnitude in intensity and

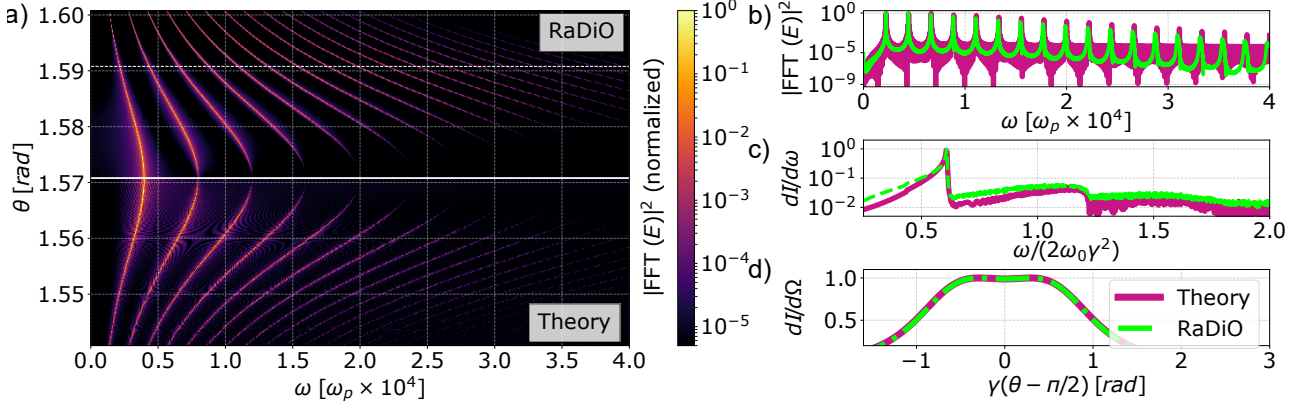


**Figure 9:** a) Comparison between the theoretical expectations for the radiated spectrum and the Post-processing code results for the radiated spectrum. b) Comparison between a lineout at  $\Delta\theta = 0.02$  from both spectra. Panels c) and d) feature the comparison between the angle and frequency integrated spectra, respectively. The detector had a temporal resolution of  $1.33 \times 10^{-5} \omega_p^{-1}$ .

brightness in synchrotron devices. In such conditions the expected spectrum is given by [10]:

$$\frac{d^2I}{d\omega d\Omega} = \frac{q_e^2 \omega^2 K^2}{\pi^2 c \omega_\beta^2 \gamma^2} \sum_{n=1}^{+\infty} \left[ J_n'^2(x) + \left( \frac{\gamma\theta}{K} - \frac{n}{x} \right)^2 J_n^2(x) \right] \times \frac{\sin^2 N\pi \left( \frac{\omega}{\omega_c} - n \right)}{\left( \frac{\omega}{\omega_c} - n \right)^2} \quad (7)$$

Where  $J_n$  is the Bessel function and  $J_n'$  its derivative, the index  $n$  corresponds to the order of the harmonic.  $N$  is the number of periods on the trajectory. Furthermore, Equation (7) is only valid for  $N \gg 1$ . Both the critical frequency  $\omega_c$  and the variable  $x$  have different definitions in this context:

$$\omega_c = \frac{2\gamma^2 \omega_\beta}{1 + K^2 + \gamma^2 \theta^2}, \quad x = \frac{K\omega\theta}{\gamma\omega_\beta} \quad (8)$$

The angle integrated frequency spectrum is given by the following expression:

$$\frac{dI}{d\Omega} = \frac{4\pi N q_e^2 K^2 r}{c} \times \sum_{n=1}^{+\infty} \left[ J_n'^2(x_n) + \left( \frac{\alpha_n}{K} - \frac{n}{x_n} \right)^2 J_n^2(x_n) \right] H(\alpha_n^2) \quad (9)$$

Here, the new variables  $r$ ,  $\alpha_n$  and  $x_n$  are introduced:  $r = \omega/(2\gamma^2\omega_\beta)$  is a scaled frequency, and  $\alpha_n = \sqrt{n/r - 1 - K^2}$  and  $x_n = 2Kr\alpha_n$  are auxiliary variables.  $H$  is the Heaviside step function.

The frequency integrated angular spectrum is given by equation 10.

$$\frac{dI}{d\Omega} = \frac{N q_e^2 \omega_\beta K^2}{c} \frac{8\gamma^4}{1 + K^2 + \gamma^2 \theta^2} \times \sum_{n=1}^{+\infty} n^2 \left[ J_n'^2(x_n) + \left( \frac{\gamma\theta}{K} - \frac{n}{x_n} \right)^2 J_n^2(x_n) \right] \quad (10)$$

In what concerns the  $K$  parameter, two regimes can be identified: smaller  $K$ 's are found in tighter orbits where the pitch angle,  $K/\gamma$ , is smaller than the radiation cone aperture,  $1/\gamma$ , resulting in a single radiation cone and an angular spectrum with an on-axis maximum. Higher  $K$ 's are found on trajectories with higher pitch angle which becomes higher than the radiation cone aperture, resulting in a radiation conical surface with an on-axis dip.

The code was successfully benchmarked in both regimes, displaying excellent agreement with all three predictions. Figure 9 shows the results obtained from an electron with  $\gamma = 57.3$  undergoing an helical motion along the  $x_1$  axis with amplitude  $r_b = 0.014 c/\omega_p$  and frequency  $\omega_\beta = 1 \omega_p$  ( $K = 0.8$ ) using a spherical detector lying on the  $x_3x_1$  plane with a radius of  $10^5 c/\omega_p$  and angular aperture of 0.03 rad (512 cells).

The spectrum, which is supposed to be symmetric around the axis ( $\theta = \pi/2$ ), was obtained from the simulation results through a Fourier transform. The left panel on Figure 9 shows the direct comparison between simulation and theory in the same manner as Figure 6. The lineout at  $\Delta\theta = 0.02$  rad (Figure 9, upper-right panel) shows a perfect match between the harmonics present in both spectra, with a significant difference in the noise of both spectra as the theoretical prediction features a much higher noise baseline, which is due to the truncation of the summation of equation (7).

As for the integrated spectra, shown on the mid-right and lower-right panels of Figure 9, a much better agreement can be found with the frequency-integrated spectrum than with the angle-integrated spectrum but the overall agreement is very good. In addition to matching the theoretical prediction perfectly, the frequency integrated spectrum ( $dI/d\Omega$ ) confirms the expectations for the intensity profile when  $K < 1$ , featuring an accumulation of intensity near the axis albeit with a slight dip caused by the fact that  $K$ , despite being smaller than 1 ( $K = 0.8$ ), is still close to the unity.

Furthermore, as these benchmarks were exclusively performed with the post-processing code, an additional

benchmark of the run-time code was required. Given that the post-processing code was previously benchmarked, this additional benchmark amounted to a simple comparison between the results of both codes.

For that purpose, we ran a simple OSIRIS 3D simulation with the run-time radiation code, and then used the trajectories from this run on the post-processing version. Finally, we compared the results of both codes. The simulation contained a single species of radiative type initially bound to a sphere. The 192 particles of this species were initialized with uniform velocity along a given direction (henceforth called the *longitudinal direction*) and random perpendicular velocity shaped by the *waterbag* function. A uniform longitudinal magnetic field made the particles undergo a radiation favorable helical trajectory.

The radiation from these particles was captured using a spherical detector with one spatial dimension and one temporal dimension placed at  $R = 10^5 [c/\omega_p]$ ,  $\theta = \pi/2$  [rad], and with  $\phi$  ranging from 0 to 0.1 [rad] (1024 cells). This detector had 4096 temporal cells ranging from  $t = R/c - 25.5 [1/\omega_p]$  to  $t = R/c - 0.5 [1/\omega_p]$ .

The results from both simulation are displayed in Figure 10, which shows the two superimposed lineouts at  $\phi = 0.075$  [rad] of both detectors. As a result, the similarity between the results from both codes becomes evident.

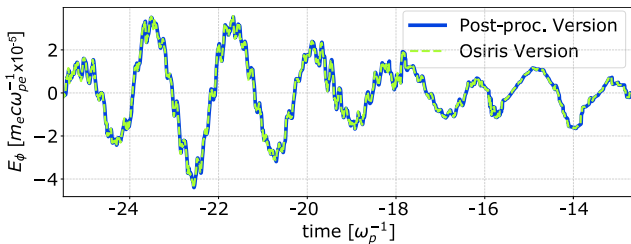


**Figure 10:** Comparison between the post-processing and run-time codes.

Overall, the benchmarks show that both versions of the code are able to provide reliable results that agree with theoretical predictions and previously well-established codes.

### 3.3. Performance

The number of operations performed by the run-time version of RaDiO should scale with  $N_{det}N_{rad}$ , where  $N_{det}$  is the number of detector spatial cells and  $N_{rad}$  is the number of radiative particles. Nevertheless, the full simulation involves running the PIC loop, which adds a factor of  $N_p + N_g$ , with  $N_p$  the number of particles in the simulation and  $N_g$  the number of grid cells.

This rough estimate can be very useful, however, apart from the fact that this assertion lacks validation, as other factors such as communications (as seldom as they may occur) might contribute to the run time, a more precise estimate is often needed. In this way, several performance tests were run with the aim of discov-

ering the actual influence of detector size and number of radiative particles on the simulation run time.

These tests consisted in ultra high resolution 3D simulations in a Thompson scattering scenario, with counter-propagating beams of electrons and light (one of each) where the computational load was varied by increasing the number of cells in the detector. Their global parameters are listed in Table 1

**Table 1:** Performance simulation parameters. Indices 1, 2 and 3 refer to the 3 spatial directions.

Parameters	Value
Box Size ( $L_1, L_2, L_3$ )	240, 0.02, 0.02 [ $c/\omega_p$ ]
No. Cells ( $n_1, n_2, n_3$ )	2400, 240, 240
Time step ( $dt$ )	0.01 [ $1/\omega_p$ ]
Simulation Time	300 [ $1/\omega_p$ ]

The number of spatial cells of this detector was varied from 0 to 128 and the number of particles was kept constant at 32840, while the simulation was run for 408320 time steps. The performance runs were performed at SuperMUC, using a maximum of 4096 cores. The results are summarized in Figure 11, which confirms the assertion that the run-time should increase linearly with  $N_{rad}N_{det}$  and quantifies the rate at which it increases: 26 core $\mu$ s/particle/detector cell/iteration. This value is higher than the one obtained for standard optimized OSIRIS simulations (with no radiative particles), reported to be of about 1 core $\mu$ s/particle/iteration. This disparity is caused by two main factors: first, unlike most OSIRIS, code the radiation is not optimized for vector operations, which leads to some decrease in performance, and secondly, despite all the efforts to optimize the radiation code, checking if the radiation falls into the timespan of the detector requires that an *if* statement be present in the innermost loop, which is highly inefficient.

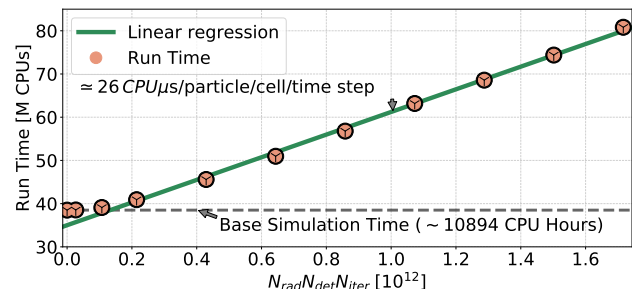


**Figure 11:** Result of the performance runs at SuperMUC. The dashed line represents the run time for runs without radiation.

### 3.4. Scalability

OSIRIS is a highly scalable code that has shown incredible performance in some of the world's largest supercomputers [11]. Therefore, in order to guarantee that this diagnostic is suitable for the OSIRIS framework it is necessary to assess its scalability.

For that purpose, we ran a strong scaling test with the run-time diagnostic which consisted in running a 2D simulation of a single radiative species with uniform density and thermal velocity together with a spherical detector with 1024 spatial cells. The most relevant simulation parameters are summarized in Table 2

**Table 2:** Scalability simulation parameters. Indices 1, 2 and 3 refer to the 3 spatial directions.

Parameters	Value
Box Size ( $L_1, L_2$ )	10, 10 [ $c/\omega_p$ ]
No. Cells ( $n_1, n_2$ )	400, 400
Time step ( $dt$ )	0.0169 [ $1/\omega_p$ ]
Simulation Time	90 [ $1/\omega_p$ ]
Particles p/ Cell	3, 3

The tests were performed at the IST Cluster, a 1560 core system, where the same simulation was run with a number of cores ranging from 40 to 640. Running the same OSIRIS simulation with radiation takes over 100 times more time than running it without radiation. This means that the contribution from number of particles dominates over the contribution from the number of grid cells, this tests mainly assess RaDiO's scalability.

The results are shown in Figure 12. It is evident that the parallel efficiency decreases with the amount of cores used, reaching a decent minimum of about 87% for 640 cores. This decrease is most likely caused by the increasing amount of communications that comes with high core counts.

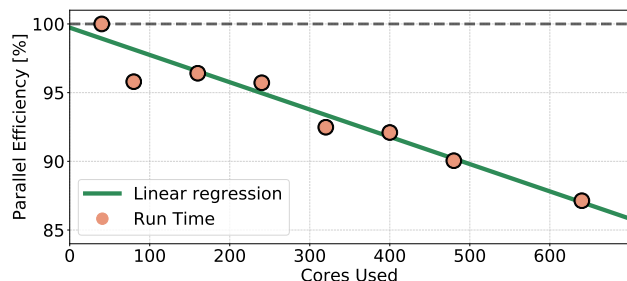


**Figure 12:** Scalability test performed at the IST cluster. The dashed line represents the ideal case.

#### 4. Radiation in Plasma Wakefield Acceleration

A highly energetic electron, proton or positron beam can drive a plasma wake capable of pushing the plasma's electrons away from the axis, creating a positively charged region, as shown in Figure 13.

Two types of fields tend to appear in that region: the acceleration field which accelerates particles in that region and the focusing field, which makes said particles undergo a sinusoidal motion [12], trapping them. This method was proposed by Chen et al. [13] in 1985, and over the past few years, numerous experiments have been conducted in order to provide the proof of concept for this method [14].

With the aim of capturing the undiscovered spa-

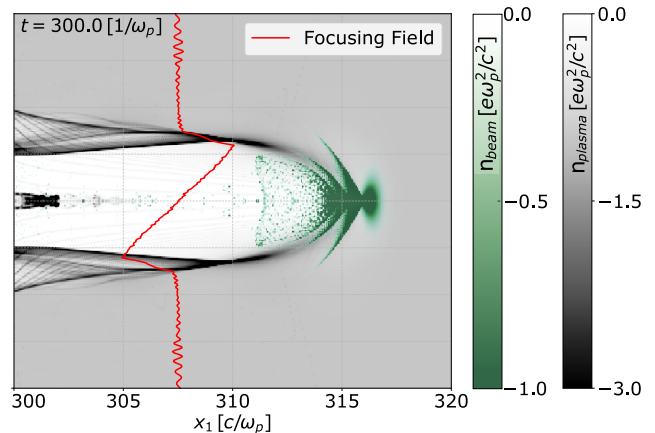


**Figure 13:** Advanced stage of the PWFA simulation. The electron beam and the background plasma are represented in green and grey, respectively. The red line represents the focusing field at  $x_1 = 307[c/\omega_p]$ .

tiotemporal signature of the radiation emitted in PWFA scenarios, several 2D simulations were performed using RaDiO. These simulations followed a highly energetic electron beam with a Gaussian density profile as it entered and traveled through a uniform plasma target. The particles in this beam that were trapped by the focusing field underwent a sinusoidal motion, emitting radiation which was captured by a slice of a spherical detector placed in the simulation plane but far from the simulation domain in the longitudinal direction ( $R = 10^6 [c/\omega_p]$ ).

The results for a time interval between  $-19.1 [1/\omega_p]$  and  $-5.0 [1/\omega_p]$  with 8192 temporal cells are shown on Figure 14. This figure displays a clear separation at  $\phi = 0$  as it seems that the transverse field,  $E_2$ , transitions from being mostly positive for  $\phi < 0$  to being mostly negative for  $\phi > 0$ , meaning that a particle in that region would suffer a net transverse acceleration. This fact is evidenced by the time averaged field on the left, which shows a symmetric field with respect to  $\phi$ . Furthermore, the emitted beam of light features a distinct tail for earlier times which corresponds to radiation emitted by the front end of the electron beam. Due to the Gaussian profile there are less particles in that region so the constructive interference is weaker for the radiation emitted in less dense regions.

In a closer inspection one can find X shaped accumulations of radiation, whose period corresponds to the cell size in the longitudinal direction, leading to the conclusion that each structure corresponds to radiation emitted by particles in the same vertical slice of the beam. Some additional but fainter X shaped structures fill the gaps between the major ones, these correspond to emissions that occurred later in the simulation, when the particles became dephased and no longer emitted coherently. Therefore, these sub-structures correspond to radiation emitted by a single particles.

The fact that it is possible to identify certain properties of the electron beam in the spatiotemporal signature of the radiation it emits suggests that it may be

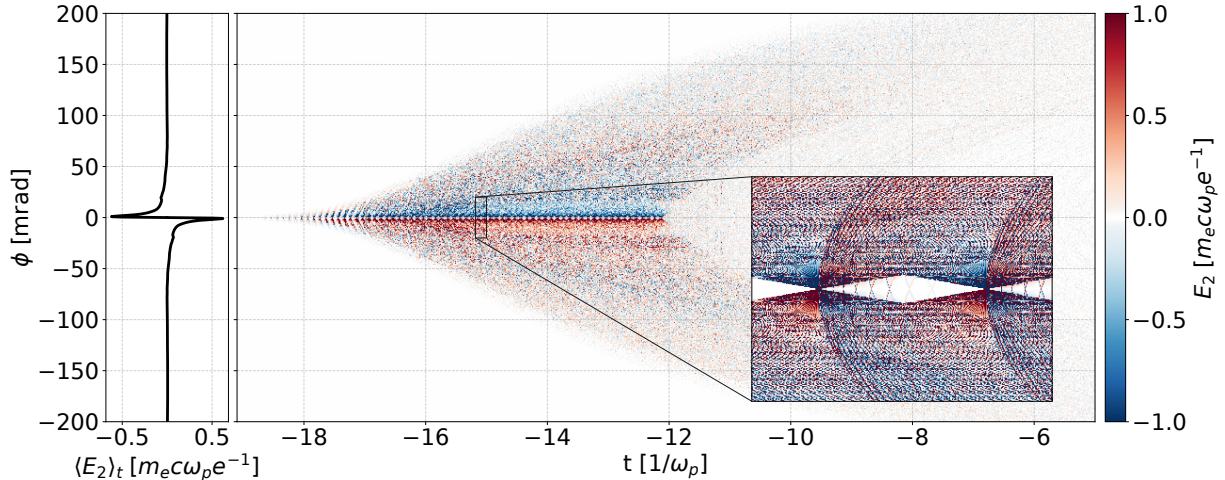


**Figure 14:** Full spatiotemporal profile of the radiation emitted by the full electron beam along the transverse direction. The time averaged field is shown on the left plot. The inset shows a close-up of the full profile.

possible to reconstruct the beam's particles trajectory from the detected light. Such study is not in the scope of this thesis, but may be relevant in future works.

### 5. The effect of macroparticles

Although the PIC algorithm allows for a significant reduction of the operations needed to simulate a plasma, one-to-one simulations are typically out of reach, as actual laboratory experiments such as the ones concerning laser plasma interaction contain a very high number of particles. Therefore, PIC codes like OSIRIS only simulate a fraction of the plasma's particles using the so-called *macroparticles*.

A macroparticle is the computational way of representing a group of particles that are assumed to move with same momentum throughout the simulation, keeping their spatial distribution static over time. This assumption is usually valid in scenarios where the collective effects dominate over the individual motion (*e.g.* laser-plasma interaction). Depending on the physical process at study, the number of particles grouped inside a macroparticle should be selected in order to ensure the validity of this approximation.

The radiation diagnostic assumes that all subparticles are concentrated in the same spot. However, as discussed by Pausch et al. [15], the shape of the macroparticle may affect the coherence of the emitted radiation. The radiated spectrum should be given by the product of the original spectrum by a shape factor:

$$\frac{d^2 I}{d\omega d\Omega} = \frac{d^2 I}{d\omega d\Omega_{\text{orig}}} [N + (N^2 - N) \mathcal{F}_\rho^2(\omega/c)] \quad (11)$$

where  $N$  is the number of subparticles inside the macroparticle and  $\mathcal{F}_\rho$  is the Fourier transform of the charge distribution inside the macroparticle,  $\rho$ . The so called cloud-in-cell (CIC) shape is one of the most commonly used for macroparticles. It consists in a uniform distribution of subparticles resulting in a rectangular function  $\Pi$  with a given width  $\sigma$ . The Fourier

transform of this shape function is the sinc function:  $\mathcal{F}_{\Pi(x)}(\omega) = \sigma/c \text{sinc}(\omega\sigma/2c)$ .

In order to simulate the effect of the macroparticles shape function on the emitted radiation the shape of the macroparticle and number of subparticles need to be specified. Then, the code computes the time of deposition for each subparticle by assuming that if the particles are distributed uniformly along space, the times at which their radiation is deposited are equally distributed along time.

The macroparticle module was tested with the same setup used in Section 3.1, but this time a CIC shape was imposed to the macroparticles, which were composed of 128 subparticles. Their width was varied from  $\sigma = 10^{-7} c/\omega_p$  to  $\sigma = 2 \times 10^{-3} c/\omega_p$ .

The spectrum was obtained through an FFT of the electric field and then integrated along the angular direction. The shape function for each  $\sigma$  was obtained by normalizing the spectra to the spectrum generated with  $\sigma = 0$ . The results are plotted in Figure 15 and it is possible to see that the shape functions clearly match the expected sinc function.

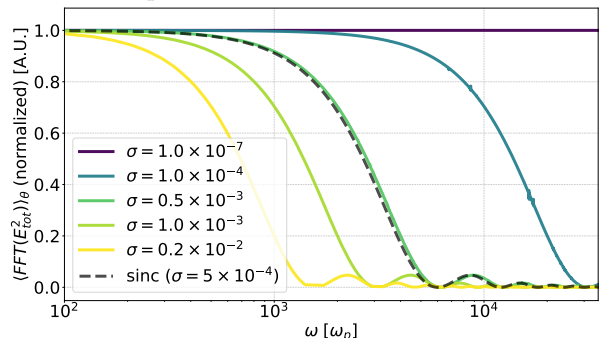


**Figure 15:** Simulated shape functions for several values of  $\sigma$ . The dashed line is the theoretical prediction for  $\sigma = 5 \times 10^{-4}$

A deeper physical insight can be given by the spatiotemporal picture of the emitted radiation. Figure 16 shows the difference between the spatiotemporal signature of a macroparticle with  $\sigma = 10^{-7} c/\omega_p$  and a

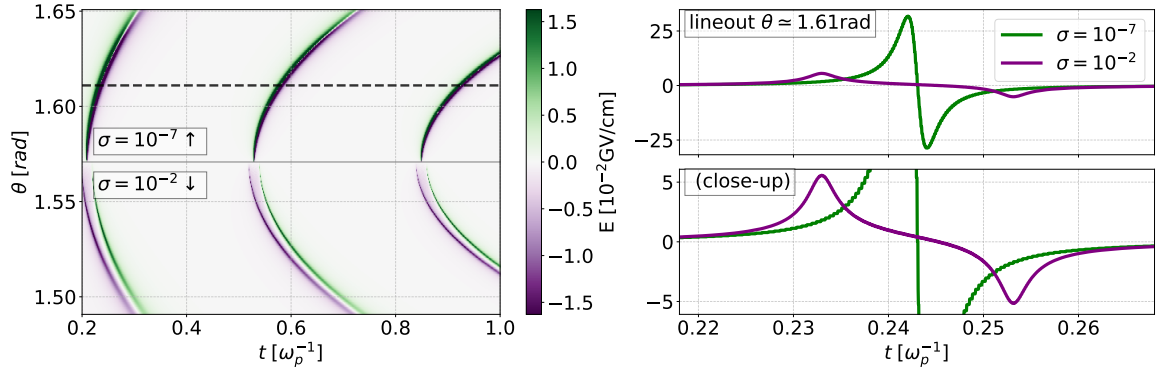


**Figure 16:** Comparison between the spatiotemporal profiles of the radiation emitted by two types of macroparticles. The left plot shows the two complementary halves of the full detector. The lineout is shown on the right panels, featuring a close-up.

macroparticle with  $\sigma = 10^{-2} c/\omega_p$ . With a smaller macroparticle, the radiation is much more intense, with shorter pulses (temporally). The opposite happens for larger macroparticles, as the radiation from each subparticle is no longer focused on the same time slot, which also leads to destructive interference. This fact is further evidenced by the lineout on the right panel of Figure 16, where the strong pulse generated by the small macroparticle becomes broader when the macroparticle becomes wider, with a much longer and less steep transition between the positive and negative parts of the pulse caused by the interference between the singular pulses of each subparticle.

## 6. Conclusions

The radiation diagnostic for OSIRIS (RaDiO) was successfully implemented, benchmarked and tested in several scenarios, including production runs. This tool offers two distinct ways of obtaining the spatiotemporal profile of radiation emitted by charged particles: either by analyzing previously obtained trajectories with the post-processing code or directly inside a PIC simulation with the code's incorporation into OSIRIS.

Both versions were implemented as parallel codes, allowing users to run this tool in the world's most powerful supercomputers. The code was put through scaling and performance tests in massive parallel systems, yielding little parallel efficiency loss even at high core counts albeit with a somewhat larger than expected computational cost for a detector with a large number of spatial cells, leaving space for future improvements.

The code was benchmarked against theoretical predictions and other well established spectral radiation codes in well known scenarios, providing solid results, and adding a high level of confidence to future runs.

RaDiO was used to probe the unexplored spatiotemporal features of radiation emitted in PWFA, which led to the conclusion the emitted radiation may accelerate far away particles and that it may be possible to infer some of the particle beam properties by assessing the periodicity of typical structures of radiation. These topics require a deeper analysis in future works.

The size and shape of the simulation macroparticles

was shown to affect the radiated spectrum, leading to a loss of coherence for higher frequencies. The results suggest that the corrected spatiotemporal profile can be obtained through Fourier filtering of the signal obtained with a point-like macroparticle.

The future work concerning this diagnostic includes its full integration into the official OSIRIS release as well as the addition of some interesting features like vector parallelization or a polarization diagnostic. As for physically relevant scenarios, apart from the ones described above, which still need further analysis, HHG was recently shown to be enhanced with spatiotemporally structured beams [16], and can thus be thoroughly studied using RaDiO.

## References

- [1] F. Tamburini et al., *Nature Physics* **7**, 195 EP (2011)
- [2] P. A. Franken et al., *Phys. Rev. Lett.* **7**, 118 (1961)
- [3] J. M. Dawson, *Rev. Mod. Phys.* **55**, 403 (1983)
- [4] J. L. Martins et al., *Proc.SPIE* **7359** (2009)
- [5] H. Bureau et al., *IEEE Transactions on Plasma Science* **38**, 10, 2831 (2010)
- [6] J. D. Jackson, *Classical Electrodynamics*, chap. 14, Wiley, 3rd ed. ed. (1999)
- [7] R. A. Fonseca et al., *OSIRIS: A Three-Dimensional, Fully Relativistic Particle in Cell Code for Modeling Plasma Based Accelerators*, 342–351, Springer Berlin Heidelberg, Berlin, Heidelberg (2002)
- [8] S. H. Glenzer et al., *Physics of Plasmas* **6**, 5, 2117 (1999)
- [9] E. Esarey et al., *Phys. Rev. E* **65**, 056505 (2002)
- [10] B. M. Kincaid, *Journal of Applied Physics* **48**, 7, 2684 (1977)
- [11] R. A. Fonseca et al., *Plasma Physics and Controlled Fusion* **55**, 12, 124011 (2013)
- [12] J. Vieira et al., *Phys. Rev. ST Accel. Beams* **14**, 071303 (2011)
- [13] P. Chen et al., *Phys. Rev. Lett.* **54**, 693 (1985)
- [14] I. Blumenfeld et al., *Nature* **445**, 741 EP (2007)
- [15] R. Pausch et al., *Proc. EAAC* (2017)
- [16] G. Gariepy et al., *Phys. Rev. Lett.* **113**, 153901 (2014)